AIMS Mathematics

http://www.aimspress.com/journal/Math

AIMS Mathematics, 5(5): 4197–4219.
DOI:10.3934/math.2020268
Received: 18 December 2019
Accepted: 10 April 2020
Published: 06 May 2020

Research article

A numerical study of the ferromagnetic flow of Carreau nanofluid over a wedge, plate and stagnation point with a magnetic dipole

H. Thameem Basha[1], **R. Sivaraj**[1,*], **A. Subramanyam Reddy**[1], **Ali J. Chamkha**[2] **and H. M. Baskonus**[3]

[1] Department of Mathematics, School of Advanced Sciences, Vellore Institute of Technology, Vellore 632014, India

[2] Mechanical Engineering Department, Prince Sultan Endowment for Energy and Environment, Prince Mohammad Bin Fahd University, Al-Khobar 31952, Saudi Arabia

[3] Department of Mathematics and Science Education, Faculty of Education, Harran University, Sanliurfa,Turkey

* **Correspondence:** Email: sivaraj.kpm@gmail.com; Tel: +918667427716.

Abstract: Present communication mainly addresses the fluid transport characteristics of ferromagnetic Carreau nanofluid over a porous wedge, plate, and stagnation point with magnetic dipole effect for shear thinning/shear thickening cases. Suitable self-similarity variables are employed to convert the fluid transport equations into ordinary differential equations which are solved with the use of the Runge-Kutta-Fehlberg (RKF) approach. To check the accuracy of the present model, numerical results for various thermophoretic values for the cases of shear thinning/shear thickening, have been compared with the results obtained by using bvp4c (MATLAB) which divulges good agreement. Influence of active parameters like ferromagnetic-hydrodynamic interaction, thermophoretic, dimensionless distance, Brownian diffusion, suction/injection, Weissenberg number are graphically presented. Computed results manifest that shear thinning and shear thickening fluids express the opposite nature in fluid velocity and temperature for higher values of Weissenberg number. Among the wedge, plate and stagnation point of the plate, the magnitude of heat transfer over the plate is significant for increasing Ferromagnetic-hydrodynamic interaction parameter. Furthermore, it is noticed that higher values of suction/injection parameter decline the fluid temperature over a plate, wedge and stagnation point of a flat plate.

Keywords: magnetic dipole; ferromagnetic flow; forced convection; Carreau nanofluid; suction/injection; wedge/plate/stagnation point
Mathematics Subject Classification: 76A05, 76R05

Nomenclature	
x, y	are the space coordinates
u, v	are the velocity components along the x and y-directions
H	is the magnetic field intensity
H_x, H_y	are the magnetic field intensities in x and y directions
C_w	is the wall concentration
C	is the fluid concentration
C_∞	is the ambient concentration
T_∞	is the ambient temperature
T_w	is the wall temperature
T	is the fluid temperature
k	is the fluid thermal conductivity
n_k	is the power law index
L_1	is the velocity slip factor
D_B	is the Brownian diffusion
D_T	is the thermophoretic diffusion
M_d	is the magnetization parameter
K_1	is the pyromagnetic coefficient
a	is the magnetic dipole distance from a surface
f_w	is the suction/injection parameter
We	is the Weissenberg number
E_C	is the Eckert number
Sc	is the Schmidt number
N_B	is the Brownian movement parameter
N_T	is the thermophoresis parameter
Pr	is the Prandtl number
C_f^*	is the dimensionless local skin friction coefficient
Nu^*	is the dimensionless local rate of heat transfer
Sh^*	is the dimensionless local rate of mass transfer
Greek symbols Nomenclature	
ν_f	is the kinematic viscosity
μ_f	is the dynamic viscosity
ρ_f	is the fluid density
Γ	is the material parameter
σ_p	is the magnetic permeability
α^*	is the thermal diffusivity
τ	is the ratio between nanoparticle and base fluid
Φ	is the magnetic scalar potential
γ_1	is the magnetic field strength
β_d	is the ferrohydrodynamic interaction parameter
α_s	is the velocity slip parameter
α_d	is the dimensionless distance
ε	is the Curie temperature
λ_d	is the viscous dissipation factor

1. Introduction

Magnetic field plays a substantial role in controlling the fluid transport characteristics which is immensely used in magnetohydrodynamic generators, high-temperature plasma, cooling of nuclear reactors and hyperthermia. Some investigation regarding magnetic field effect is quoted in the literature via [1–11]. Ferrofluid is a colloidal suspension which includes the nanosized magnetic particles and suitable base fluid. Ferrofluids exhibit regular fluid properties with the addition of strong magnetization force whose prime impacts are notably experienced in fluid temperature. Each magnetic particle coated by surfactant to control the particles cluster. Nano-sized ferromagnetic particles have a less magnetic attraction when the surfactant van der Waals force of notable strength to block magnetic cluster. Ferrofluid model is initiated by Pappell [12] at the NASA and propounded that this fluid model can be utilized as a rocket propellant. Furthermore, he has observed that the flow of this fluid may be oriented and attracted by a magnetic field. Ferrofluids have a diverse application like pressure transducers [13], ferrofluid lubrications, sensor applications, thermal management in electric motors and hi-fi speaker [14], magnet treatment of pain management, densimeter, cure arthritis, gout, MRI, treatment of cancer and tumor by a magnetic fluid [15]. Misra and shit [16] have addressed the magnetic dipole impact on biomagnetic fluid in a parallel plate and noticed that the temperature gradually inflate when boosting ferromagnetic interactions. The viscoelastic fluid flow influenced by the magnetic dipole and suction has been illustrated by Majeed et al. [17] and have observed that ferromagnetic interaction is strongly dominant in fluid flow. Muhammad and Nadeem [18] have explored the heat transfer of three different ferrite nanoparticles in ethylene glycol base fluid over a sheet and have depicted that the three different ferrite nanofluids have reduced the wall shear stress.

When the shear stress and shear rate of the fluid are nonlinear, the fluid becomes non-Newtonian. Numerous works regarding the fluid transport properties of non-Newtonian fluids have been published in recent decades because such fluids have widespread applications in biological materials (blood, saliva), chemical materials (polymer fluids, pharmaceutical chemicals), food processing (ketchup, yogurt), flow in journal bearings, solar collectors, etc. Several non-Newtonian models like micropolar fluid, Maxwell fluid, Cross fluid, Walter's B-fluid and Casson fluid have been proposed to model the fluid flow in several realistic situations. All the non-Newtonian fluids can't be explored using a single constitutive relationship because different non-Newtonian fluids have diverse fluid characteristics. It is to be noted that these fluids are categorized into rate, differential and integral types. Carreau fluid (the combination of Newtonian fluid and power-law properties) is one of rate type fluids and this model was proposed by Carreau [19]. It is to be noted that this fluid expresses shear thinning, shear thickening and Newtonian properties for $n = 0$, $0 < n < 1$, and $n > 1$, respectively. Carreau fluid model has received notable attention due to its significance in tumors treatment, cosmetics [20], bitumen for road construction [21], extrusion of a polymer [22], etc. Khan et al. [23] have utilized Buongiorno nanofluid model to explore the time-dependent Carreau nanofluid over a wedge and have found that the shear thinning fluid Weissenberg number enhances the fluid temperature. Waqas et al. [24] have investigated the two different characteristics of Carreau nanofluid with the influence of magnetic field. Khan et al. [25] have studied the fluid transport properties of hydromagnetic Carreau nanofluid over a 3D extending sheet for solar energy application.

Nanofluids are obtained by a suspension of high thermal conductivity nano-size particles ($CNT's$,

CuO and Al_2O_3) in low thermal conductivity fluids (water, oil, ethylene glycol). Such a new class of high heat transfer fluids was first proposed by Choi et al. [26]. In the past few years, numerous experimental and theoretical studies have been carried out to enhance the thermal conductivity of nanofluids as a result of inevitable applications such as oil coolers, internal coolers for compressors, CPU cooling, power generation, and solar collectors. Though numerous models have been introduced to study the nanofluids, the Buongiorno model is one of the nanofluid models, which is adopted by many researchers to analyze the nanofluids. Buongiorno [27] model consists of the momentum, heat and mass transport equations with the influence of Brownian motion and thermophoretic diffusivity. Khan et al. [28] have utilized the Buongiorno nanofluid model to explore fluid transport properties and entropy generation of tangent hyperbolic nanofluid with nonlinear convection and have observed that varying thermophoretic parameter enhances temperature and mass transfer of nanofluid. Ghadikolaei et al. [29] have scrutinized the impact of nonlinear radiation on magneto Eyring-Powell nanofluid by using Buongiorno nanofluid model and have found that increasing values of Brownian motion parameter declines the mass transfer. Lin and Jiang [30] have numerically investigated the Newtonian and non-Newtonian base fluid with copper nanoparticle over a circular groove in the presence of Brownian motion and thermophoresis.

Prandtl have originated the boundary layer theory to determine the flow of a fluid on a solid surface. A parallel flow over a horizontal flat plate in the presence of constant velocity was first initiated by Blasius. Later, Falkner and Skan [31] have made a model for a non-parallel flow direction based on the theory that Prandtl have developed. They have introduced a parameter β (pressure gradient) which plays a vital role to change the direction of the fluid velocity. It is observed that velocity field has an inflection point at $\beta < 0$ and there is no inflection point at $\beta > 0$. Falkner-Skan flow model has received notable attention from the researchers due to its applications in different fields like wire drawing, oil exploration, drawing of plastic films, geothermal industries, and nuclear reactors. Many researchers have studied the Falkner-Skan flow for static and moving wedge. Lin and Lin [32] have examined the Falkner-Skan flow over a wedge, plate, and stagnation of a flat plate and have introduced a parameter to investigate the transport properties of the fluids with any fluid Prandtl number. Nadeem et al. [33] have investigated the influence of the induced magnetic field on the water nanofluid over a wedge and have found that the flow of a fluid over a moving wedge ($\lambda = 0.3$) is higher compared to fluid flow over a static wedge ($\lambda = 0$). Hendi and Hussain [34] have employed an analytical method to investigate the hydromagnetic Falkner-Skan flow over a porous wedge and have observed that the fluid velocity declines for injecting the fluid via porous surface. Alam et al. [35] have explored the effect of variable viscosity on Falkner-Skan flow of an incompressible fluid over a porous wedge and have noticed that the fluid temperature reduces for injecting the fluid. Further studies on Falkner-Skan flow of nanofluid over a wedge can be found in [36–39].

Previously, researchers have investigated the magnetic dipole effect on plate and stretching sheet cases with various non-Newtonian fluid models. In the present model, we have examined the magnetic dipole effect on three different geometry cases with shear-thinning/shear-thickening characteristics of Carreau fluid. From a significant review of the current literature, it is known that no attempt has been made to investigate the Carreau nanofluid over three different geometries in the presence of magnetic dipole, thermophoresis and Brownian motion. The Falkner-Skan flow of Carreau nanofluid with the magnetic dipole and suction/injection may be useful to improve the performance of solar energy. Governing equations are modeled by using Buongiorno nanofluid

model. It is to be noted that the employed similarity transformation is suitable for any fluid Prandtl number. RK Fehlberg method is adopted as a computational tool for characterizing the non-dimensional governing equations. Influence of diverse pertinent parameters on the velocity, temperature and concentration are analyzed through the graphs.

2. Mathematical formulation

We consider two-dimensional (x, y) Falkner-Skan flow of a ferromagnetic Carreau nanofluid over a porous wedge, plate and stagnation point of flat plate as demonstrated in Figure 1. It is assumed that the velocity of the potential flow away from the boundary layer is $u_\infty = bx^m$ where b is the constant. Here, $m = \frac{\beta_1}{2-\beta_1}$ is the Hartree pressure gradient. $\beta_1 = 0, 0.5$ and 1 represent the flow over a plate, wedge and stagnation point of a flat plate, respectively. The magnetic dipole is implemented in the x-axis and this leads to generate the magnetic field. The temperature (T_w) and concentration (C_w) of the wall is fixed and they are higher than the ambient temperature (T_∞) and ambient concentration (C_∞), respectively.

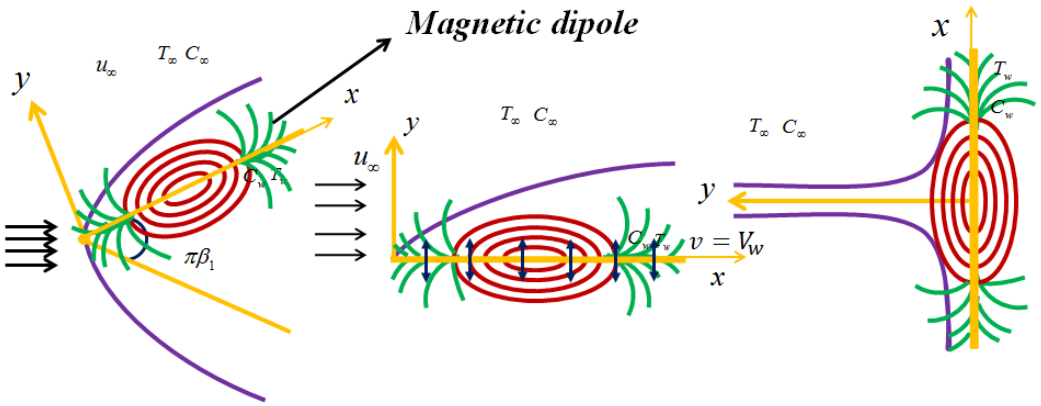

Figure 1. Physical configuration of the problem.

Based on the above settings, the flow assumptions are

- Laminar, steady, incompressible, forced convective flow of ferromagnetic Carreau nanofluid is considered.
- The body force is neglected in the momentum equation.
- fluid flow has a slip behavior.
- The surface can inject/suck the fluid.
- Buongiorno nanofluid model is employed to model the governing equations.

Within the framework of the aforementioned suppositions, the governing equations are [16,22,23,32]

$$\frac{\partial u}{\partial x} + \frac{\partial v}{\partial y} = 0, \tag{2.1}$$

$$u\frac{\partial u}{\partial x} + v\frac{\partial u}{\partial y} = u_\infty \frac{du_\infty}{dx} + \nu_f \frac{\partial^2 u}{\partial y^2}\left[1 + \Gamma^2\left(\frac{\partial u}{\partial y}\right)^2\right]^{\frac{n_k-1}{2}}$$

$$+\nu_f\,(n_k-1)\,\Gamma^2\frac{\partial^2 u}{\partial y^2}\left(\frac{\partial u}{\partial y}\right)^2\left[1+\Gamma^2\left(\frac{\partial u}{\partial y}\right)^2\right]^{\frac{n_k-3}{2}}+\frac{\sigma_p}{\rho_f}M_d\left(\frac{\partial H}{\partial x}\right), \tag{2.2}$$

$$u\frac{\partial T}{\partial x}+v\frac{\partial T}{\partial y}=\alpha^*\frac{\partial^2 T}{\partial y^2}-\frac{\sigma_p}{\left(\rho C_p\right)_f}T\frac{\partial M_d}{\partial T}\left(u\frac{\partial H}{\partial x}+v\frac{\partial H}{\partial y}\right)$$

$$+\tau\left[D_B\frac{\partial T}{\partial y}\frac{\partial C}{\partial y}+\frac{D_T}{T_\infty}\left(\frac{\partial T}{\partial y}\right)^2\right], \tag{2.3}$$

$$u\frac{\partial C}{\partial x}+v\frac{\partial C}{\partial y}=D_B\frac{\partial^2 C}{\partial y^2}+\frac{D_T}{T_\infty}\frac{\partial^2 T}{\partial y^2}. \tag{2.4}$$

The boundary conditions are [23,36,38,39]

$$u=L_1\left(\frac{\partial u}{\partial y}\right)\left[1+\Gamma^2\left(\frac{\partial u}{\partial y}\right)^2\right]^{\frac{n_k-1}{2}},\ v=V_w,\ T=T_w,$$

$$D_B\frac{\partial C}{\partial y}+\frac{D_T}{T_\infty}\frac{\partial T}{\partial y}=0 \qquad \text{at y} = 0,$$

$$u=u_\infty,\ T\to T_\infty, C\to C_\infty \qquad \text{as y}\to\infty. \tag{2.5}$$

where $\nu_f=\frac{\mu_f}{\rho_f}$, $\alpha^*=\frac{k_f}{\left(\rho C_p\right)_f}$, $\tau=\frac{\left(\rho C_p\right)_p}{\left(\rho C_p\right)_f}$.

Magnetic scalar potential (Φ) portrays the magnetic dipole region, which is expressed as [16,17]

$$\Phi=\frac{\gamma_1}{2\pi}\frac{x}{x^2+(y+a)^2}, \tag{2.6}$$

where γ_1 is the magnetic field strength and the components of magnetic field (H) are H_x and H_y in x and y directions which are expressed as,

$$H_x=-\frac{\partial\Phi}{\partial x}=\frac{\gamma_1}{2\pi}\frac{x^2-(y+a)^2}{\left(x^2+(y+a)^2\right)^2}, \tag{2.7}$$

$$H_y=-\frac{\partial\Phi}{\partial y}=\frac{\gamma_1}{2\pi}\frac{2x(y+a)}{\left(x^2+(y+a)^2\right)^2}, \tag{2.8}$$

Intensity of magnetic field (H) is given by

$$H=\left[\left(\frac{\partial\Phi}{\partial x}\right)^2+\left(\frac{\partial\Phi}{\partial y}\right)^2\right]^{0.5}, \tag{2.9}$$

Eqs (2.7) and (2.8) become

$$\frac{\partial H}{\partial x}=-\frac{\gamma_1}{2\pi}\frac{2x}{(y+a)^4}, \tag{2.10}$$

$$\frac{\partial H}{\partial y} = -\frac{\gamma_1}{2\pi}\frac{2}{(y+a)^3} + \frac{\gamma_1}{2\pi}\frac{4x^2}{(y+a)^5}, \tag{2.11}$$

The changes of M_d in terms of temperature is given by

$$M_d = K_1(T - T_\infty), \tag{2.12}$$

A parameter λ is given by Lin and Lin [32] which is used to study the fluid transport properties with any fluid Prandtl number, $\lambda = \delta\sqrt{\mathrm{Re}}$, where $\mathrm{Re} = \frac{u_\infty x}{\nu}$ is Reynolds number, $\delta = \frac{\sqrt{\mathrm{Pr}}}{(1+\mathrm{Pr})^n}$, $n = \frac{1}{6}$ for plate, wedge and stagnation of flat plate.

Suitable self-similarity variables are introduced as follows:

$$\begin{cases} \eta = \left(\frac{y}{x}\right)\lambda, \\ f(\eta) = \frac{\psi(x,y)}{\alpha^* \lambda}, \\ u = \frac{f'(\eta) b x^m}{(1+\mathrm{Pr})^{2n}}, \\ v = -\left(\frac{\alpha^*}{x}\right)\lambda\left[\frac{m+1}{2} f(\eta) + \frac{m-1}{2}\eta f'(\eta)\right], \\ V_w = -\left(\frac{\alpha^*}{x}\right)\lambda\left[\frac{m+1}{2} f_w\right], \\ T = (T_w - T_\infty)\,\theta(\eta) + T_\infty, \\ C = (C_w - C_\infty)\,\chi(\eta) + C_\infty. \end{cases} \tag{2.13}$$

We have employed the aforesaid suitable self-similarity variables (2.13) for non-dimensionalization and parameterization of the momentum equation (2.2), temperature equation (2.3) and concentration equation (2.4) subject to the boundary conditions (2.5)

$$\begin{aligned} &\mathrm{Pr}\, f'''\left[1 + n_k\, We^2 (f'')^2 \left(\frac{\mathrm{Pr}}{(1+\mathrm{Pr})^{6n}}\right)\right] \\ &\left[1 + \ We^2 (f'')^2 \left(\frac{\mathrm{Pr}}{(1+\mathrm{Pr})^{6n}}\right)\right]^{\frac{n_k-3}{2}} - \frac{2\beta_d \theta \mathrm{Pr}^2}{\left[\eta + \alpha_d\left(\frac{\sqrt{\mathrm{Pr}}}{(1+\mathrm{Pr})^n}\right)\right]^4} \\ &+ \left(\frac{m+1}{2}\right) f f'' + m\left((1+Pr)^{4n} - (f')^2\right) = 0, \end{aligned} \tag{2.14}$$

$$\begin{aligned} &\theta'' + \mathrm{Pr}\, N_B \theta' \chi' + \mathrm{Pr}\, N_T (\theta')^2 + \left(\frac{m+1}{2}\right) f\, \theta' \\ &- \frac{\beta_d\, \lambda_d\, (\theta+\varepsilon)}{(1+\mathrm{Pr})^{2n}}\left[\frac{2\left(\left(\frac{m+1}{2}\right) f + \left(\frac{m-1}{2}\right)\eta f'\right)}{\left[\eta + \alpha_d\left(\frac{\sqrt{\mathrm{Pr}}}{(1+\mathrm{Pr})^n}\right)\right]^3}\right] + \frac{E_C\, \beta_d\, \mathrm{Pr}^2\, (\theta+\varepsilon)}{(1+\mathrm{Pr})^{4n}} \\ &\left[\frac{2 f'}{\left[\eta + \alpha_d\left(\frac{\sqrt{\mathrm{Pr}}}{(1+\mathrm{Pr})^n}\right)\right]^4} + \frac{4\left(\left(\frac{m+1}{2}\right) f + \left(\frac{m-1}{2}\right)\eta f'\right)}{\left[\eta + \alpha_d\left(\frac{\sqrt{\mathrm{Pr}}}{(1+\mathrm{Pr})^n}\right)\right]^5}\right] = 0, \end{aligned} \tag{2.15}$$

$$\chi'' + \left(\frac{m+1}{2}\right) f \chi' \ \frac{\mathrm{Sc}}{\mathrm{Pr}} + \frac{N_T}{N_B}\theta'' = 0. \tag{2.16}$$

along with the transformed boundary conditions

$$\begin{aligned} f(\eta) = f_w,\ f'(\eta) = \frac{\sqrt{\Pr}\,\alpha_s f''(\eta)}{(1+\Pr)^n}\left[1 + We^2(f''(\eta))^2\frac{\Pr}{(1+\Pr)^{6n}}\right]^{\frac{n_k-1}{2}}, \\ \theta(\eta) = 1\,,\ N_B\chi'(\eta) + N_T\theta'(\eta) = 0 \qquad \text{at } \eta = 0, \\ f'(\eta) = (1+\Pr)^{2n}, \qquad \theta(\eta) \to 0, \quad \chi(\eta) \to 0 \qquad \text{as } \eta \to \infty. \end{aligned} \tag{2.17}$$

where $We = \sqrt{\frac{\Gamma^2 b^3 x^{3m}}{\nu_f\, x}}$, $\beta_d = \frac{\sigma_\rho \rho_f \gamma_1 K_1 (T_w - T_\infty)}{2\pi\mu_f^2}$, $\alpha_s = L_1\sqrt{\frac{bx^{m-1}}{\nu_f}}$, $\alpha_d = \sqrt{\frac{bx^{m-1}\rho_f a^2}{\mu_f}}$, $E_C = \frac{u_\infty^2}{(C_p)_f(T_w - T_\infty)}$, $\varepsilon = \frac{T_\infty}{T_w - T_\infty}$, $\lambda_d = \frac{bx^{m-1}\mu_f^2}{k_f\rho_f(T_w - T_\infty)}$, $\Pr = \frac{\nu_f}{\alpha^*}$, $N_B = \frac{\tau D_B(C_w - C_\infty)}{\nu_f}$, $N_T = \frac{\tau D_T(T_w - T_\infty)}{T_\infty \nu_f}$ and $Sc = \frac{\nu_f}{D_B}$.

The dimensionless local skin friction coefficient $\left(C_f^*\right)$, dimensionless local rate of heat transfer (Nu^*) and dimensionless local rate of mass transfer (Sh^*) at the wall are defined as

$$\begin{cases} C_f^* \mathrm{Re}^{1/2} = \dfrac{f''(0)\sqrt{\Pr}\left(1 + \frac{We^2\,\Pr\,(f''(0))^2}{(1+\Pr)^{6n}}\right)^{\frac{n_k-1}{2}}}{\sqrt{1+\Pr}}, \\ Nu^* \mathrm{Re}^{1/2}\delta^{-1} = -\theta'(0)\,, \\ Sh^* \mathrm{Re}^{1/2}\delta^{-1} = -\chi'(0)\,. \end{cases} \tag{2.18}$$

3. Numerical method and code validation

The dimensionless equations (2.14)–(2.16) and corresponding boundary conditions (2.17) have been solved by using 4^{th} and 5^{th} order RK Fehlberg scheme. In this approach, the boundary value problem (BVP) is converted into an initial value problem (IVP). Some investigation for solving the partial differential equations are coated in the literature via [40–48].

$$\frac{\overline{y_{m+1}} - \overline{y_m}}{h} = t_0\frac{25}{216} + t_2\frac{1408}{2565} + t_3\frac{2197}{4109} - t_4\frac{1}{5} \tag{3.1}$$

$$\frac{\overline{y_{m+1}} - \overline{y_m}}{h} = t_0\frac{16}{135} + t_2\frac{6656}{12825} + t_3\frac{28561}{56430} - t_4\frac{9}{50} + \frac{2}{55}t_5, \tag{3.2}$$

where (3.1) and (3.2) are the 4^{th} and 5^{th} order approximations to the solution respectively, and also;

$$\begin{cases} \frac{t_0}{f} = \overline{x_m} + \overline{y_m}, \\ \frac{t_1}{f} = \overline{x_m} + \frac{h}{4}, \overline{y_m} + \frac{ht_0}{4}, \\ \frac{t_2}{f} = \overline{x_m} + \frac{3h}{8}, \overline{y_m} + \frac{3ht_0}{32} + \frac{9ht_1}{32}, \\ \frac{t_3}{f} = \overline{x_m} + \frac{12h}{13}, \overline{y_m} + \frac{1932ht_0}{2197} - \frac{7200ht_1}{2197} + \frac{7296ht_2}{2197}, \\ \frac{t_4}{f} = \overline{x_m} + h, \overline{y_m} + \frac{439ht_0}{216} - 8ht_1 + \frac{3860ht_2}{513} - \frac{845ht_3}{4104}, \\ \frac{t_5}{f} = \overline{x_m} + \frac{h}{2}, \overline{y_m} - \frac{8ht_0}{27} + 2ht_1 - \frac{3544ht_2}{2565} + \frac{1859ht_3}{4104} - \frac{11ht_4}{40}, \end{cases} \tag{3.3}$$

below mentioned new set of variables are employed for computation:

$$\left.\begin{aligned} f = a_1,\ f' = a_2,\ f'' = a_3,\ f''' = a_3' \\ \theta = a_4,\ \theta' = a_5, \chi = a_6,\ \chi' = a_7 \end{aligned}\right\} \tag{3.4}$$

applying Eq (3.4) in Eqs (2.14)–(2.16) to obtain the following reduced equations;

$$\begin{aligned}
&\mathrm{Pr}\, a_3{}'\left[1+n_k\, We^2(a_3)^2\left(\frac{\mathrm{Pr}}{(1+\mathrm{Pr})^{6n}}\right)\right]\\
&\left[1+\ We^2(a_3)^2\left(\frac{\mathrm{Pr}}{(1+\mathrm{Pr})^{6n}}\right)\right]^{\frac{n_k-3}{2}}-\frac{2\beta_d a_4\mathrm{Pr}^2}{\left[\eta+\alpha_d\left(\frac{\sqrt{\mathrm{Pr}}}{(1+\mathrm{Pr})^n}\right)\right]^4}\\
&+\left(\frac{m+1}{2}\right)a_1\, a_3+m\left((1+Pr)^{4n}-(a_2)^2\right)=0, \qquad (3.5)\\
&a_5{}'+\mathrm{Pr}\, N_B a_5\, a_7+\mathrm{Pr}\, N_T(a_5)^2+\left(\frac{m+1}{2}\right)a_1\, a_5\\
&-\frac{\beta_d\,\lambda_d\,(a_4+\varepsilon)}{(1+\mathrm{Pr})^{2n}}\left[\frac{2\left(\left(\frac{m+1}{2}\right)a_1+\left(\frac{m-1}{2}\right)\eta a_2\right)}{\left[\eta+\alpha_d\left(\frac{\sqrt{\mathrm{Pr}}}{(1+\mathrm{Pr})^n}\right)\right]^3}\right]+\frac{E_C\,\beta_d\,\mathrm{Pr}^2\,(a_4+\varepsilon)}{(1+\mathrm{Pr})^{4n}}\\
&\left[\frac{2\,a_2}{\left[\eta+\alpha_d\left(\frac{\sqrt{\mathrm{Pr}}}{(1+\mathrm{Pr})^n}\right)\right]^4}+\frac{4\left(\left(\frac{m+1}{2}\right)a_1+\left(\frac{m-1}{2}\right)\eta a_2\right)}{\left[\eta+\alpha_d\left(\frac{\sqrt{\mathrm{Pr}}}{(1+\mathrm{Pr})^n}\right)\right]^5}\right]=0, \qquad (3.6)\\
&a_7{}'+\left(\frac{m+1}{2}\right)a_1\, a_7\ \frac{\mathrm{Sc}}{\mathrm{Pr}}+\frac{N_T}{N_B}a_5{}'=0. \qquad (3.7)
\end{aligned}$$

with the boundary conditions

$$\begin{aligned}
a_1(\eta)=f_w,\ a_2(\eta)=\ &\frac{\sqrt{\mathrm{Pr}}\,\alpha_s a_3(\eta)}{(1+\mathrm{Pr})^n}\left[1+We^2(a_3(\eta))^2\frac{\mathrm{Pr}}{(1+\mathrm{Pr})^{6n}}\right]^{\frac{n_k-1}{2}},\\
a_4(\eta)=1\,,\ N_B a_7(\eta)+N_T a_5(\eta)=0 \qquad &\text{at}\ \ \eta=0,\\
a_2(\eta)=(1+\mathrm{Pr})^{2n},\qquad a_4(\eta)\to 0,\qquad a_6(\eta)\to 0 \qquad &\text{as}\ \ \eta\to\infty. \qquad (3.8)
\end{aligned}$$

The step size in the numerical solution is fixed as 0.001 ($\eta = 0.001$) and ten-decimal 1×10^{-10} places accuracy is fixed for the criterion of convergence. To check the validity of the present model, the numerical results are compared with bvp4c and Lin and Lin [32] which are given in Tables 1–3. Bvp4c is a MATLAB package that provides the solution using the 3-stage Lobatto IIIa formula and the finite difference scheme. Besides, suitable initial guesses are required to obtain a better solution. It is noticed that the procedures of this solver are clearly expressed in Shampine et al. [49]. Furthermore, many researchers are widely employed bvp4c solver to solve boundary value problems [36,37]. The comparison results reported in Tables 1–3 have received a good agreement. This evidences that the adopted numerical simulation gives the precise results.

Table 1. Comparison result of Nu^* with bvp4c for Shear thinning Carreau nanofluid.

	$Nu^*\mathrm{Re}^{-1/2}\delta^{-1}$					
	Shear thinning					
Parameter	Plate		Wedge		Stagnation point	
N_T	RKF Method	bvp4c (MATLAB)	RKF Method	bvp4c (MATLAB)	RKF Method	bvp4c (MATLAB)
0.1	0.391052	0.391052	0.543891	0.543892	0.801992	0.801993
0.3	0.350035	0.350035	0.481822	0.481824	0.710629	0.710630
0.5	0.309662	0.309663	0.419365	0.419365	0.618605	0.618606
0.8	0.250594	0.250595	0.324974	0.324974	0.479210	0.479211
1.0	0.212516	0.212517	0.261846	0.261846	0.385652	0.385652

Table 2. Comparison result of Nu^* with bvp4c for Shear thickening Carreau nanofluid.

	$Nu^*\mathrm{Re}^{-1/2}\delta^{-1}$					
	Shear thickening					
Parameter	Plate		Wedge		Stagnation point	
N_T	RKF Method	bvp4c (MATLAB)	RKF Method	bvp4c (MATLAB)	RKF Method	bvp4c (MATLAB)
0.1	0.388573	0.388573	0.536379	0.536379	0.793714	0.793714
0.3	0.346855	0.346855	0.472941	0.472942	0.699411	0.699412
0.5	0.305795	0.305795	0.409335	0.409336	0.604878	0.604878
0.8	0.245756	0.245757	0.313825	0.313825	0.462948	0.462949
1.0	0.207105	0.207106	0.250524	0.250524	0.368883	0.368884

Table 3. Comparison result of Nu^* in the absences of We, β_d, α_s, α_d, E_c, N_B, N_T,ε and Sc with the results of Lin and Lin [32] and bvp4c.

Pr	Plate			Wedge			Stagnation point		
	RKF Present	Lin and Lin [32]	bvp4c	RKF Present	Lin and Lin [32]	bvp4c	RKF Present	Lin and Lin [32]	bvp4c
0.01	0.51675	0.51675	0.51681	0.61440	0.61437	0.61435	0.76098	0.76098	0.76098
0.1	0.44997	0.44991	0.44993	0.55926	0.55922	0.55922	0.70524	0.70524	0.70524
1	0.37293	0.37272	0.37281	0.49401	0.49396	0.49396	0.64032	0.64032	0.64032
10	0.34371	0.34338	0.34356	0.47824	0.47703	0.47947	0.63192	0.63136	0.63192

4. Results and discussion

The aim of this section is to exhibit the graphical outcomes of active parameters on the velocity(f'), temperature(θ), concentration(χ), skin friction factor, rate of heat transfer and rate of mass transfer for shear thinning and shear thickening nature of ferromagnetic Carreau nanofluid. Calculations have been made for distinct values of f_w=0, 0.5, 1, α_d= 1.3, 1.4, 1.5, β_d=0.5, 1.0, 1.5, N_B=0.2, 0.4, 0.6, N_T=0.1, 0.3, 0.5, We=1, 3, 5 and Pr = 21. The solutions of non-linear equations are obtained numerically by using RK Fehlberg method. All the graphs display the shear thinning ($n_k < 1$) and shear thickening ($n_k > 1$) nature of ferromagnetic Carreau nanofluid. Solid, dashdot, dash lines in order represent the shear thinning and shear thickening Carreau nanofluid characteristics over a plate, wedge, and stagnation point of the plate. Figures 2–16 depict the characteristics of fluid transport properties, Figure 17 presents the streamlines of velocity and Figures 18–23 illustrate the rate of heat transfer for the wedge, plate and stagnation point of the plate.

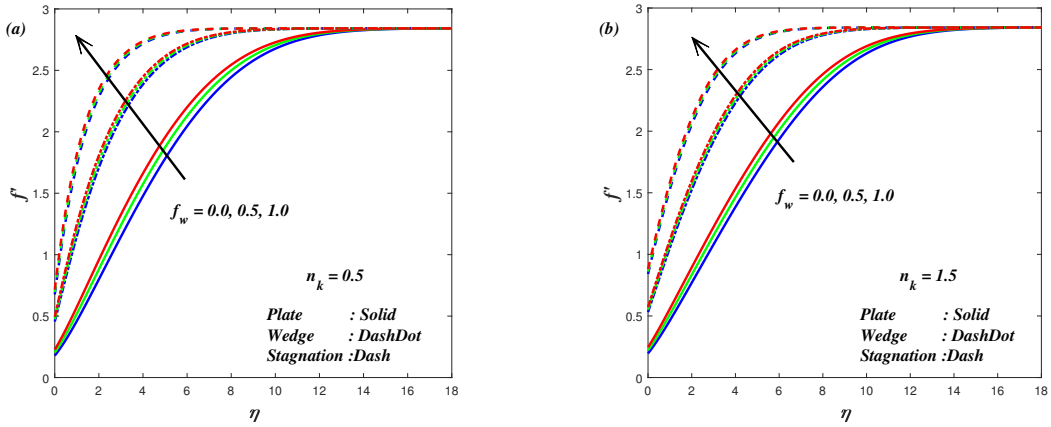

Figure 2. Plot of f' for increasing f_w.

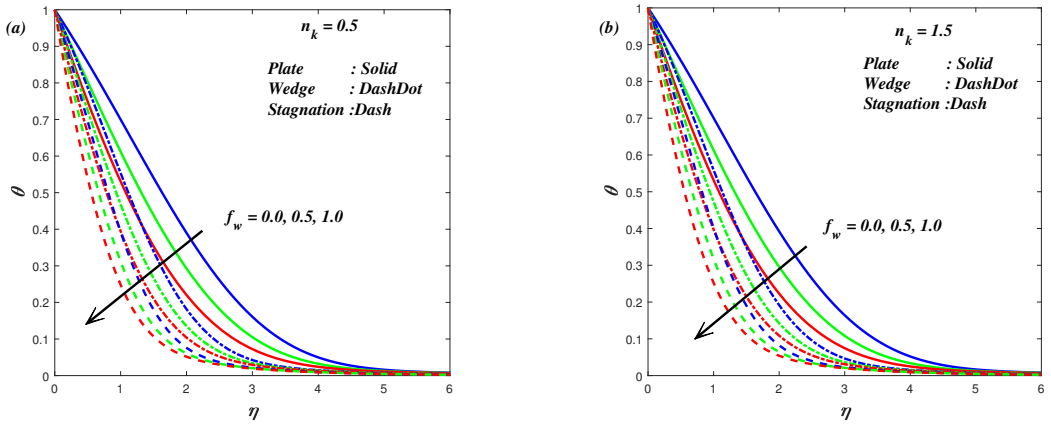

Figure 3. Plot of θ for increasing f_w.

Figures 2 and 3 are depicted to manifest the impact of f_w for shear thinning and shear thickening cases of ferromagnetic Carreau nanofluid on f' and θ, respectively. Variation of f' against f_w is displayed in Figure 2. This figure displays that $n_k < 1$ as well as $n_k > 1$ has high velocity when the

fluid is injected through a surface. Further, it is noticed that the velocity is higher for $n_k < 1$ than $n_k > 1$. θ is portrayed for increasing the values of f_w in Figure 3. It is noticed that the higher values of f_w diminish the boundary layer thickness of θ over the plate, wedge, and stagnation point. This is due to the fact that θ declines with an escalation in f_w. It is also observed that the stagnation point of a flat plate has a low temperature compared with the plate and wedge.

Figures 4 and 5 exhibit the influence of α_d on f' and θ for two different natures of ferromagnetic Carreau nanofluid namely shear thinning and shear thickening, respectively. An increasing trend in f' is depicted for higher values of α_d. The influence of viscous forces declines when the fluid moves away from magnetic dipole, thus the fluid velocity is increasing. Due to the distance from the magnetic dipole, center experiences a decay in the temperature of the fluid. Figures 6 and 7 elucidate the impact of We on $f'$and θ, respectively. It is evident from these figures that larger values of We in $n_k < 1$ increase f' but decrease θ, on the other hand the reverse trend is observed for $n_k > 1$. It is also noticed that the velocity and thermal related boundary layer thickness are the decaying function of We in $n_k < 1$ however quite reverse behavior is observed in $n_k > 1$.

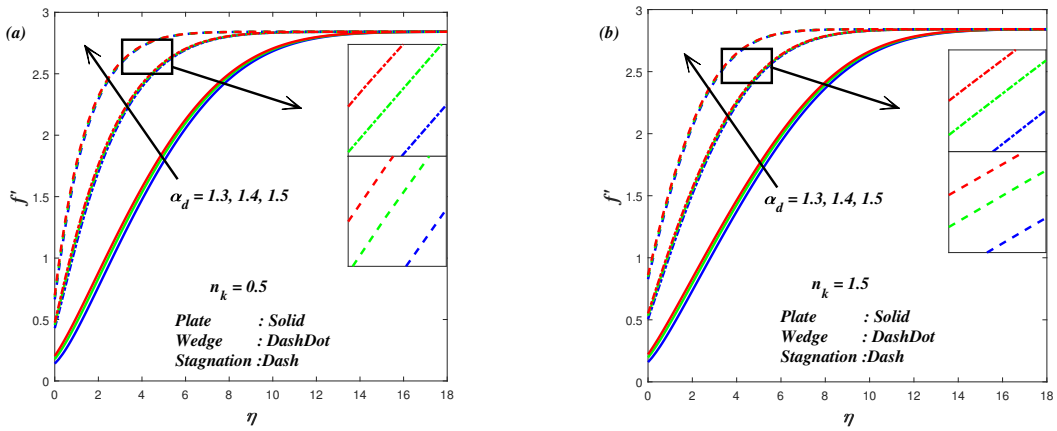

Figure 4. Plot of f' for increasing α_d.

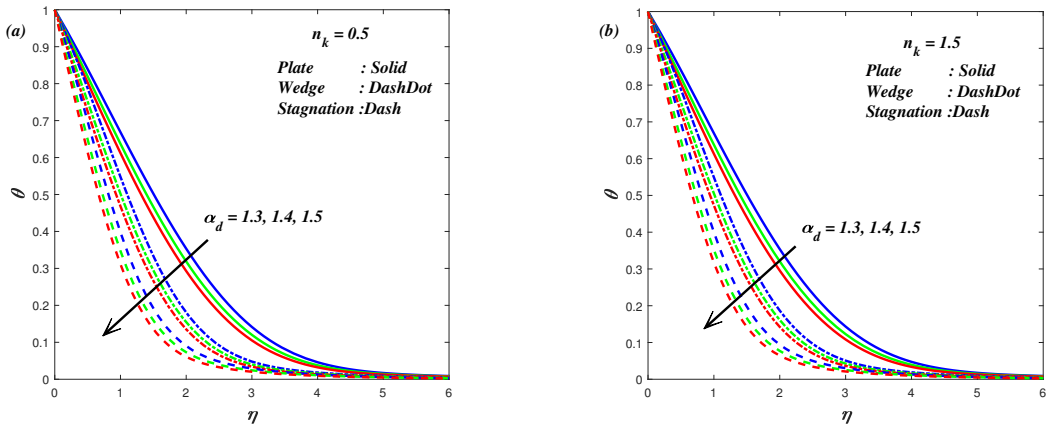

Figure 5. Plot of θ for increasing α_d.

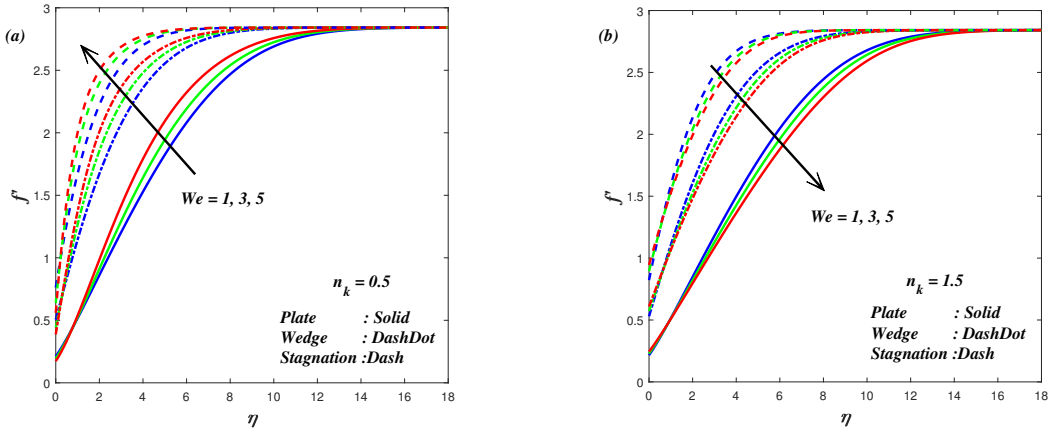

Figure 6. Plot of f' for increasing We.

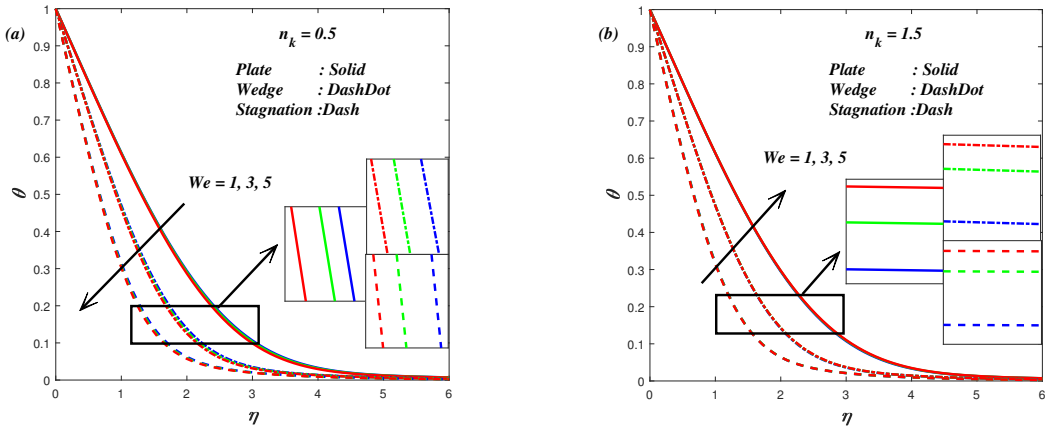

Figure 7. Plot of θ for increasing We.

Figures 8 and 9 are plotted to explore the impact of β_d on f' and θ of the shear thinning and shear thickening fluid cases, respectively. It is seen that f' reduces for larger values of β_d. Physically, the magnetic field behaves as an opposing force in the fluid flow when β_d raises. Figure 9 portrays how β_d affects θ. This figure shows that θ is enhanced for higher values of β_d. This is due to the interaction between the fluid transport and action of the magnetic particles. Furthermore, this interaction reduces the velocity of the fluid so that frictional heat increases between the fluid layers, thus the thermal related boundary layer thickness is increasing.

Figures 10 and 11 demonstrate the effect of N_T on θ and χ for $n_k < 1$ and $n_k > 1$ cases, respectively. The thermophoretic force is generated as a result of the temperature gradient which leads to rapid the flow over the plate, wedge and stagnation point of the plate. As a result, the thermal related boundary layer rises with an increasing value of N_T. Variation of N_T on χ is illustrated in Figure 11. It is evident from this figure that χ increases with higher values of N_T. The thermophoresis force triggers the nanoparticles to move from hot surface to cold surface which causes the mass related boundary layer thickness to upsurge. Figure 12 displays the results for shear thinning and shear thickening nanofluids χ for distinct values of N_B. It is seen from the figure that χ shows a decreasing behavior over the plate, wedge and stagnation point of the plate as N_B increases. Brownian movement occurs in nanofluid

system due to contact of nanoparticles with the base fluid. This leads to enhance the heat conduction and hence the concentration boundary layer thickness diminishes.

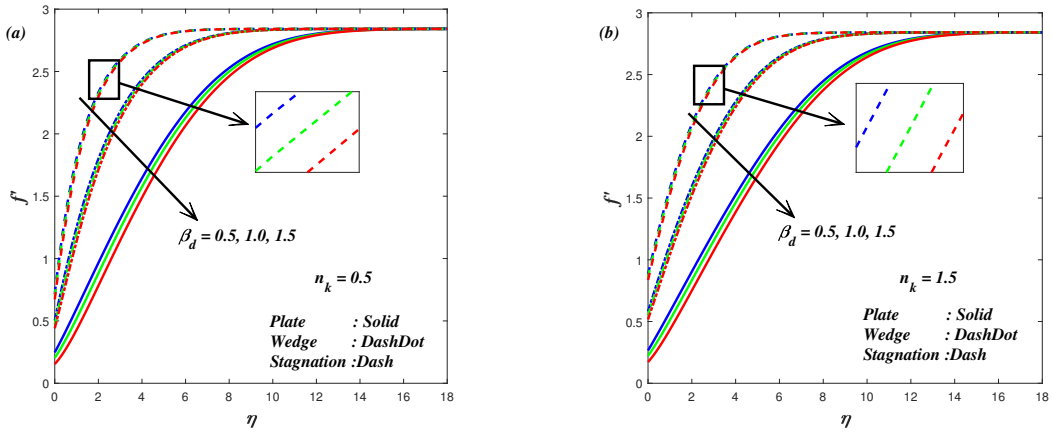

Figure 8. Plot of f' for increasing β_d.

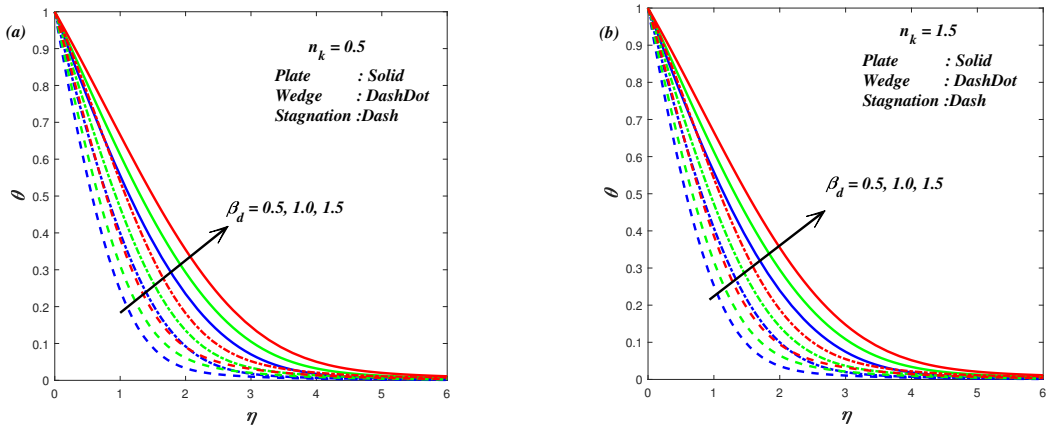

Figure 9. Plot of θ for increasing β_d.

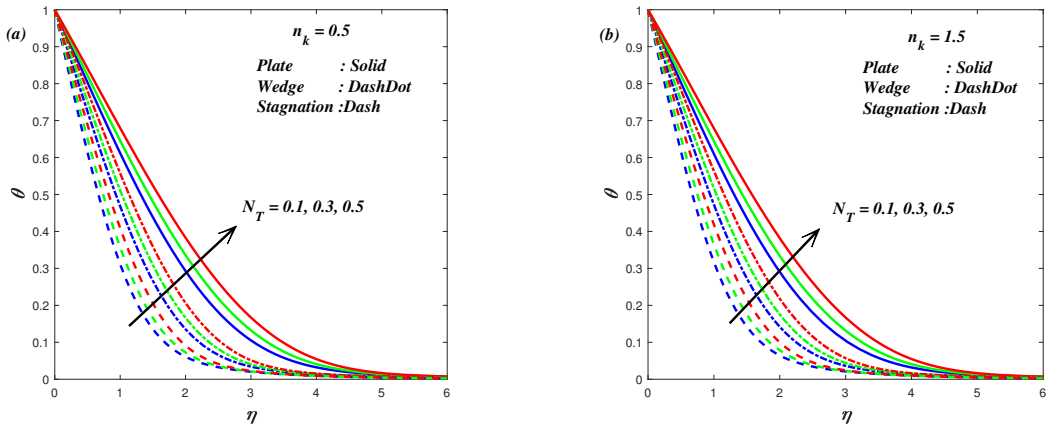

Figure 10. Plot of θ for increasing N_T.

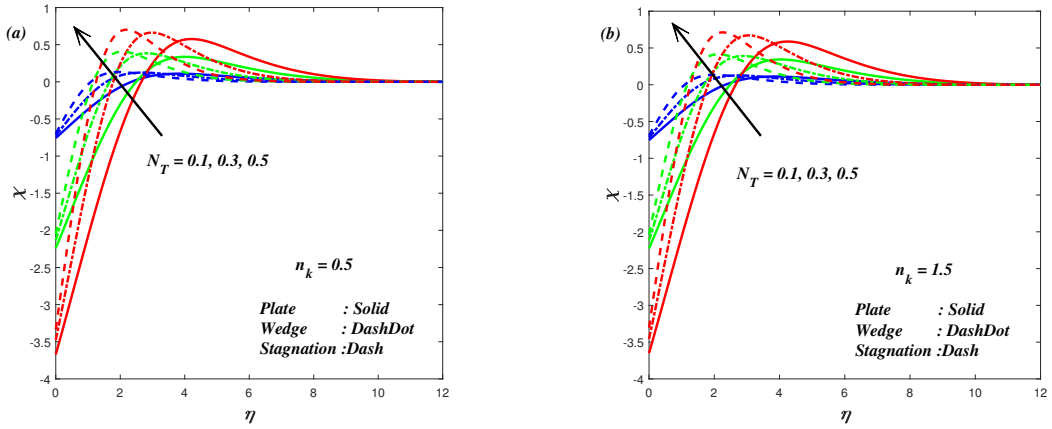

Figure 11. Plot of χ for increasing N_T.

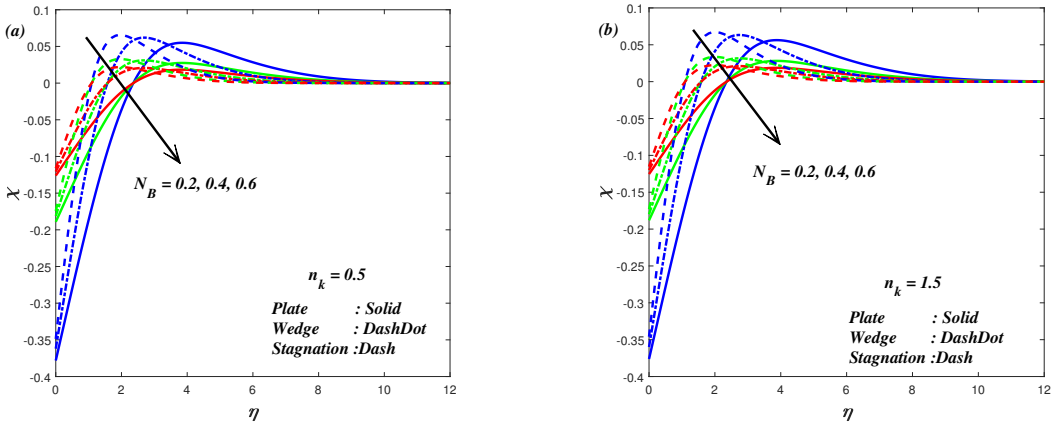

Figure 12. Plot of χ for increasing N_B.

The consequences of α_s on C_f^* along with We is analyzed in Figure 13. It is observed that C_f^* of shear thinning fluid at the surface reduces by augmenting We but the opposite nature is observed in shear thickening fluid. It is shown that an increase in the values of α_s highly reduces C_f^* over a stagnation point case for both shear thinning and shear thickening nanofluids. Figure 14 is drawn to explore the influence of N_T for $n_k < 1$ and $n_k > 1$ on N_u^* against α_d. It is noticed that N_u^* of nanofluid at the surfaces of the plate, wedge and stagnation point increases for enhancing values of α_d. However, an increase in N_T restricts the augments of N_u^* at the surface. The impacts of E_C and β_d on N_u^* are elucidated in Figure 15. It is observed that N_u^* decreases for the given values of β_d. Also, it is revealed that E_C causes to decline N_u^* for $n_k < 1$ and $n_k > 1$. Figure 16 displays the influences of N_T and N_B parameters on the rate of mass transfer. It is evident from this figure that the rate of mass transfer increases at the surface by enhancing N_B. It is also noticed that N_T declines the rate of mass transfer. Figure 17 elucidates the flow pattern over the plate, wedge and stagnation point for both the cases $n_k < 1$ and $n_k > 1$ of Carreau nanofluid in the absence of f_w. Figures 18–23 elucidate the characteristics of Nu^* for various values of E_C and β_d over the plate, wedge and stagnation point for $n_k < 1$ as well as $n_k > 1$. It is clear that an enhancement in E_C result in an elevation in the internal source of energy which enhances the thermal boundary layer, as a result, the Nusselt number decreases for higher values of E_C and β_d.

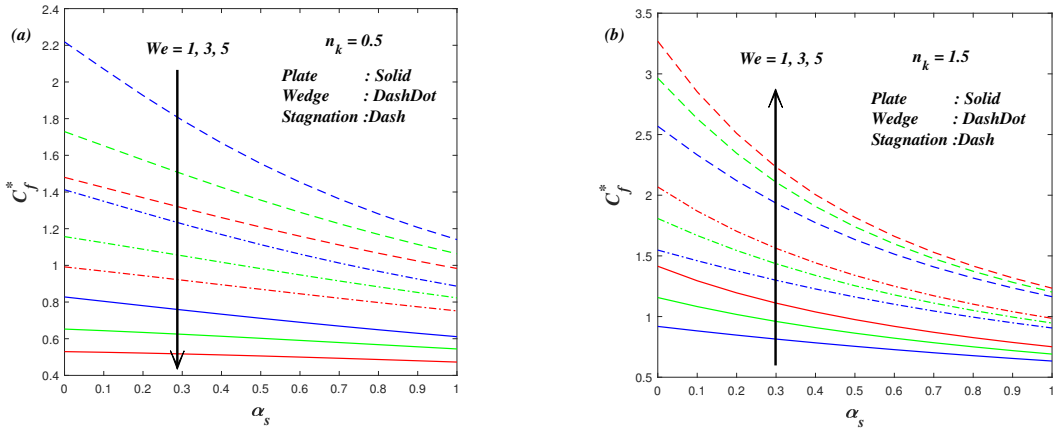

Figure 13. Plot of C_f^* for increasing α_S and We.

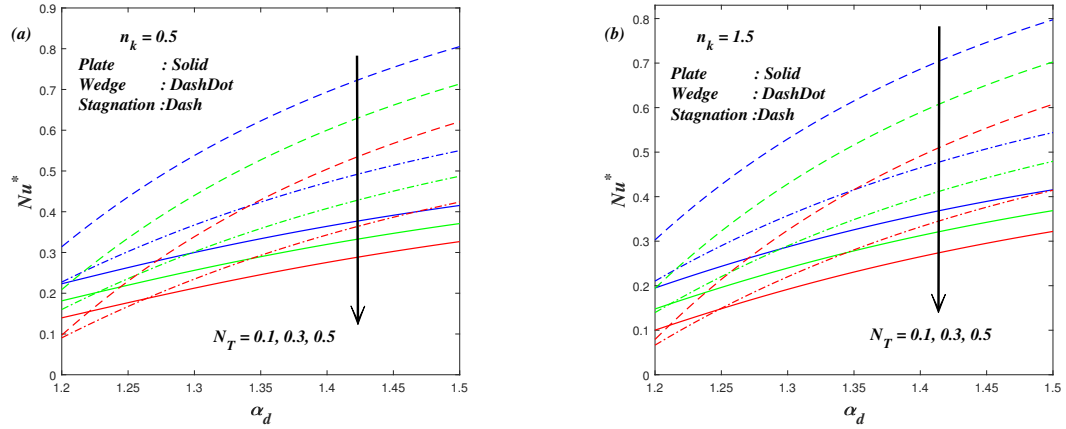

Figure 14. Plot of Nu^* for increasing α_d and N_T.

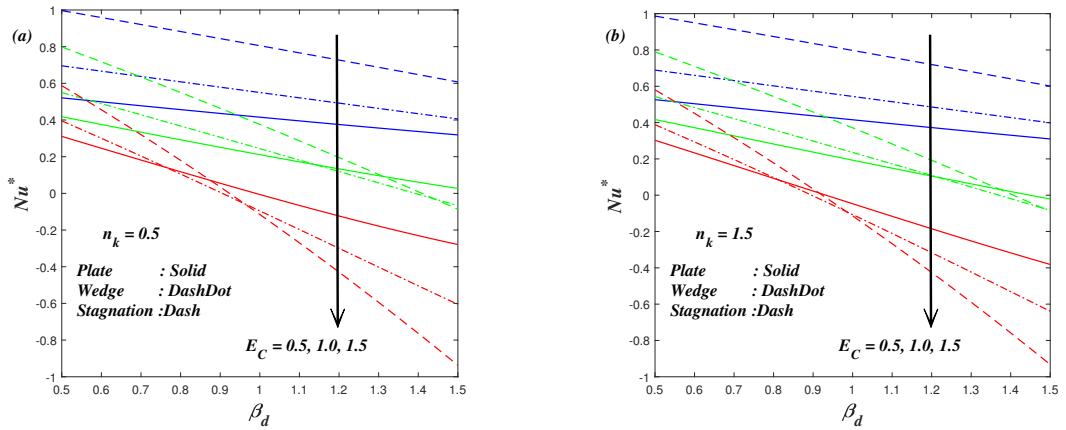

Figure 15. Plot of Nu^* for increasing β_d and E_C.

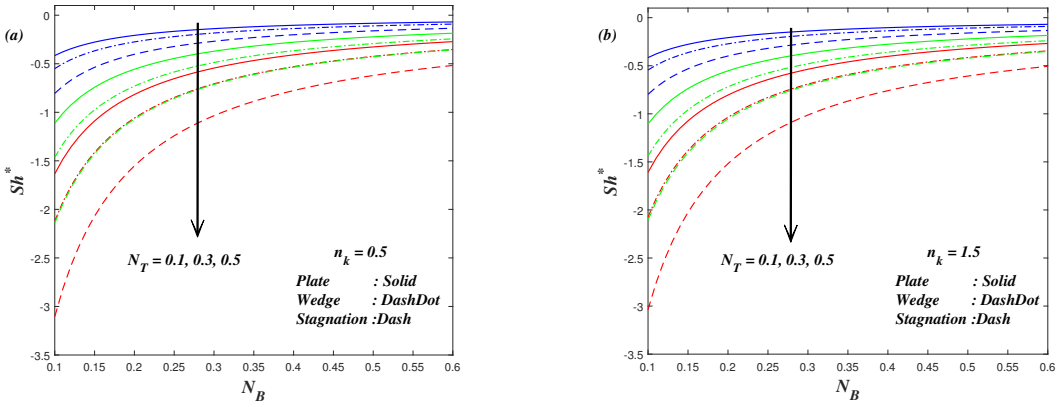

Figure 16. Plot of Sh^* for increasing N_B and N_T.

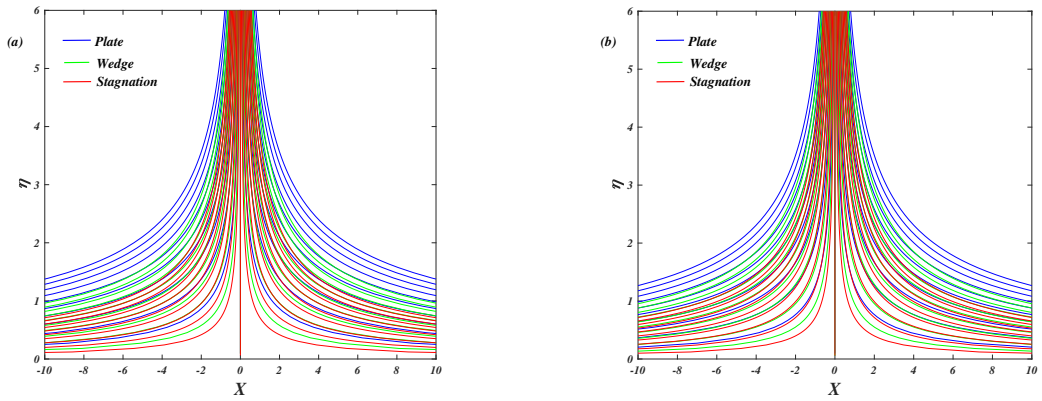

Figure 17. Velocity flow pattern for shear thinning and shear thickening characteristics of Carreau nanofluid in the absence of suction/injection.

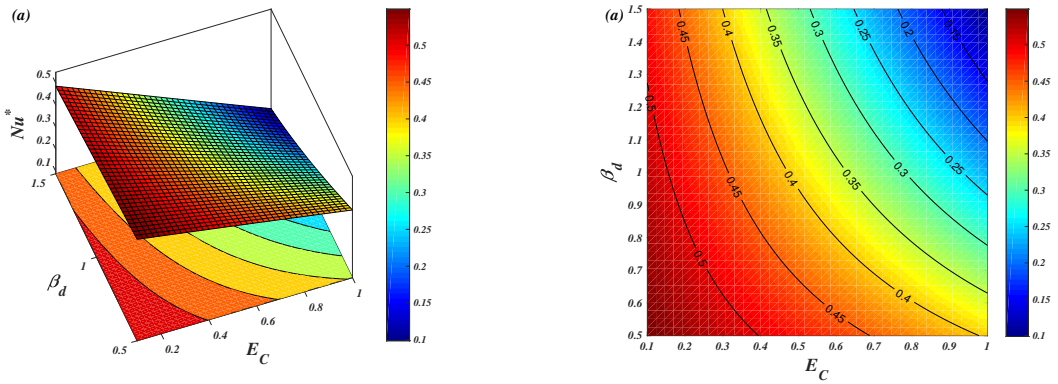

Figure 18. 3D plot and contour with the impact of E_C and β_d on Nu^* for shear thinning Carreau nanofluid when $\beta_1 = 0$.

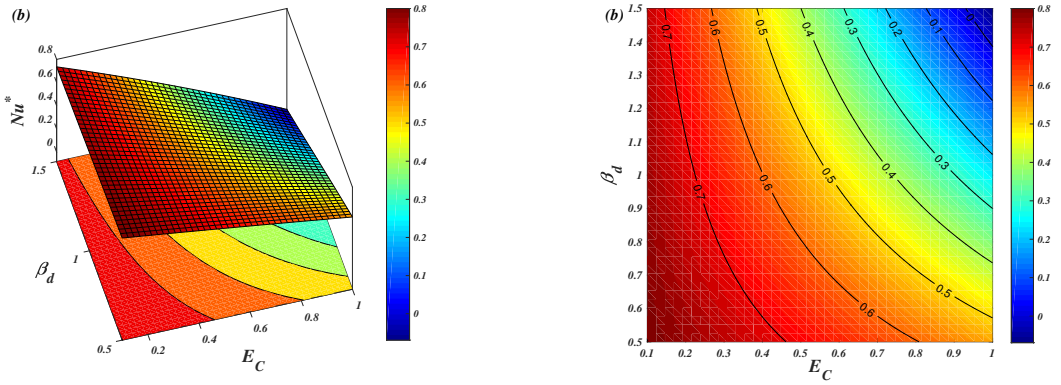

Figure 19. 3D plot and contour with the impact of E_C and β_d on Nu^* for shear thinning Carreau nanofluid when $\beta_1 = 0.5$.

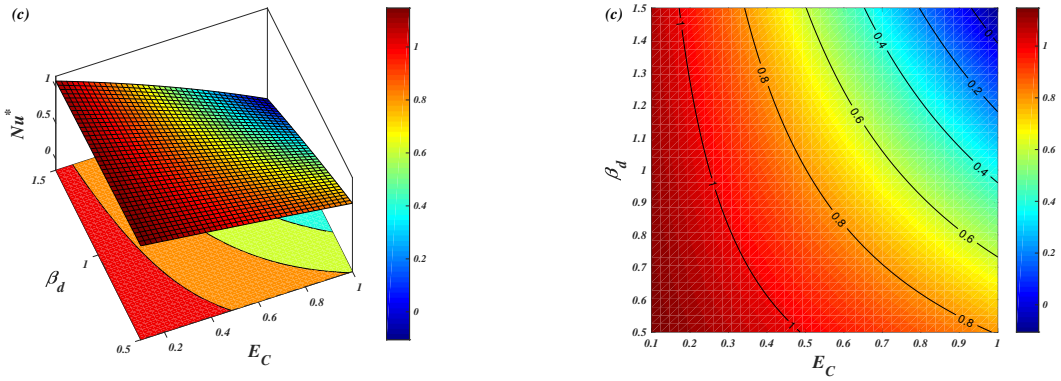

Figure 20. 3D plot and contour with the impact of E_C and β_d on Nu^* for shear thinning Carreau nanofluid when $\beta_1 = 1$.

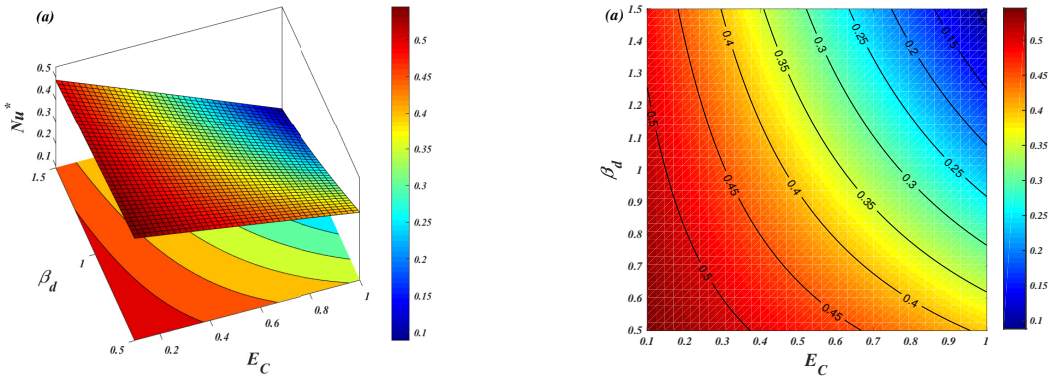

Figure 21. 3D plot and contour with the impact of E_C and β_d on Nu^* for shear thickening Carreau nanofluid when $\beta_1 = 0$.

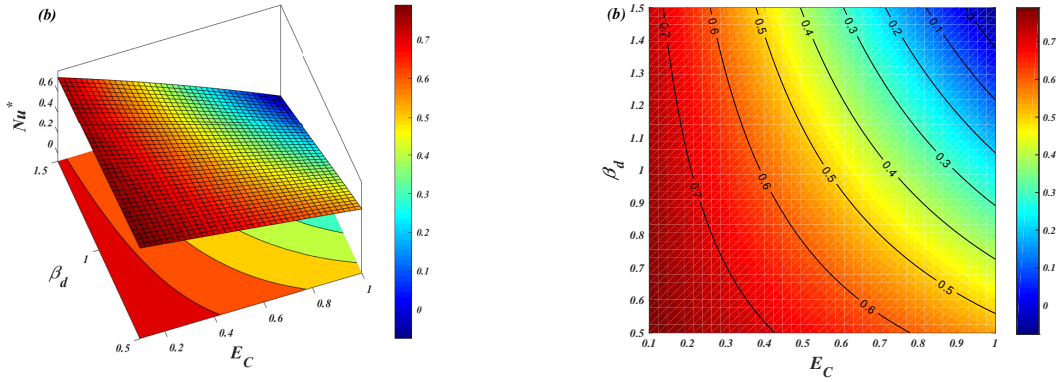

Figure 22. 3D plot and contour with the impact of E_C and β_d on Nu^* for shear thickening Carreau nanofluid when $\beta_1 = 0.5$.

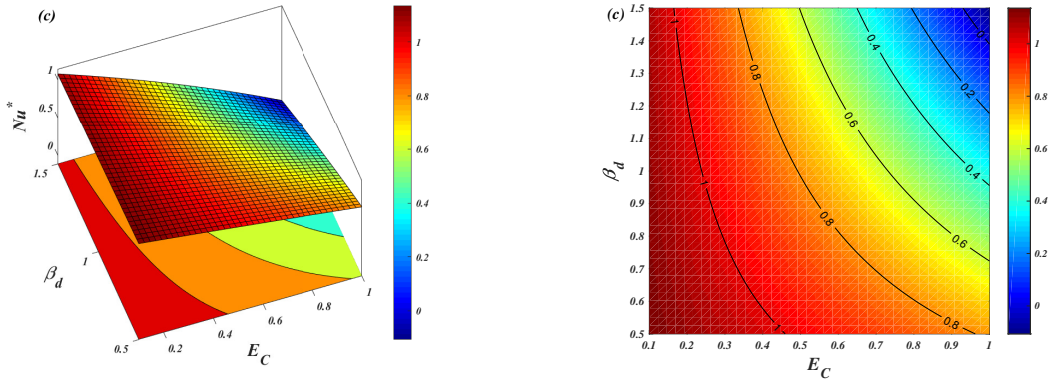

Figure 23. 3D plot and contour with the impact of E_C and β_d on Nu^* for shear thickening Carreau nanofluid when $\beta_1 = 1$.

5. Conclusion

This analysis contains a numerical solution for forced convective Falkner-Skan flow of ferromagnetic Carreau nanofluid flow over the plate, wedge and stagnation point of a flat plate with the influence of magnetic dipole and suction/injection. The present study may be used to increase the efficiency of the solar energy system. The outcomes are demonstrated in terms of 2-dimensional plot, streamlines, 3-dimensional surface plot and contour plot. Some notable observations from this analysis are summarised as follows:

- The impact of Weissenberg number on shear thinning/shear thickening nanofluid has a reverse behavior on velocity and temperature distributions.
- As suction/injection rises which leads to increase the fluid velocity but decreases the temperature of the fluid.
- The temperature of shear thinning/shear thickening nanofluid increases with an increase in thermophoretic and ferromagnetic-hydrodynamic interaction.
- An increment of Brownian motion tends to decline the fluid concentration.

- The shear thinning fluid has slightly higher temperature than shear thickening fluid.
- Among the wedge, plate, and stagnation point of a flat plate, the fluid flow over plate experiences less skin friction factor for both shear thinning and shear thickening nanofluids.
- Shear thinning nanofluid and shear thickening nanofluid have a low rate of heat transfer over plate among wedge, plate and stagnation point of a flat plate.

Conflict of interest

On behalf of all authors, the corresponding author states that there is no conflict of interest.

References

1. R. Sivaraj, B. R. Kumar, *Unsteady MHD dusty viscoelastic fluid Couette flow in an irregular channel with varying mass diffusion*, Int. J. Heat Mass Tran., **55** (2012), 3076–3089.
2. B. R. Kumar, R. Sivaraj, *Heat and mass transfer in MHD viscoelastic fluid flow over a vertical cone and flat plate with variable viscosity*, Int. J. Heat Mass Tran., **56** (2013), 370–379.
3. B. R. Kumar, R. Sivaraj, *MHD viscoelastic fluid non-Darcy flow over a vertical cone and a flat plate*, Int. Commun. Heat Mass Tran., **40** (2013), 1–6.
4. A. J. Benazir, R. Sivaraj, M. M. Rashidi, *Comparison between Casson fluid flow in the presence of heat and mass transfer from a vertical cone and flat plate*, J. Heat Trans., **138** (2016), 1–6.
5. Z. Li, A. Shafee, M. Ramzan, et al. *Simulation of natural convection of Fe_3O_4-water ferrofluid in a circular porous cavity in the presence of a magnetic field*, Eur. Phys. J. Plus, **134** (2019), 77.
6. P. Besthapu, R. Ul Haq, S. Bandari, et al. *Thermal radiation and slip effects on MHD stagnation point flow of non-Newtonian nanofluid over a convective stretching surface*, Neural Comput. Appl., **31** (2019), 207–217.
7. F. A. Soomro, R. Ul Haq, Q. M. Al-Mdallal, et al. *Heat generation/absorption and nonlinear radiation effects on stagnation point flow of nanofluid along a moving surface*, Results Phys., **8** (2018), 404–414.
8. K. Ur Rehman, I. Shahzadi, M. Y. Malik, et al. *On heat transfer in the presence of nano-sized particles suspended in a magnetized rotatory flow field*, Case Stud. Therm. Eng., **14** (2019), 1–10.
9. P. Ragupathi, A. K. A. Hakeem, Q. M. Al-Mdallal, et al. *Non-uniform heat source/sink effects on the three-dimensional flow of Fe_3O_4 /Al_2O_3 nanoparticles with different base fluids past a Riga plate*, Case Stud. Therm. Eng., **15** (2019), 1–9.
10. S. Saranya, P. Ragupathi, B.Ganga, et al. *Non-linear radiation effects on magnetic/non-magnetic nanoparticles with different base fluids over a flat plate*, Adv. Powder Technol., **29** (2018), 1977–1990.
11. S. Aman, Q. Al-Mdallal, *Flow of ferrofluids under second order slip effect*, AIP Conference Proceedings, **2116** (2019), 030012.
12. S. S. Papell, *Low viscosity magnetic fluid obtained by colloidal suspension of magnetic particles*, U. S. Patent, **215** (1965), 572.

13. K. Raj, R. Moskowitz, *Commercial applications of ferrofluids*, J. Magn. Magn. Mater., **85** (1990), 233–245.

14. D. B. Hathaway, *Use of ferrofluid in moving coil loudspeakers*, dB-sound Eng. Mag., **13** (1979), 42–44.

15. M. I. I. Shliomis, *Comment on "Ferrofluids as Thermal Ratchets"*, Phys. Rev. Lett., **92** (2004) 188902.

16. J. C. Misra, G. C. Shit, *Flow of a biomagnetic visco-elastic fluid in a channel with stretching walls*, J. Appl. Mech., **76** (2015), 1–9.

17. A. Majeed, A. Zeeshan, R. Ellahi, *Unsteady ferromagnetic liquid flow and heat transfer analysis over a stretching sheet with the effect of dipole and prescribed heat flux*, J. Mol. Liq., **223** (2016), 528–533.

18. N. Muhammad, S. Nadeem, *Ferrite nanoparticles Ni-$ZnFe_2O_4$, Mn-$ZnFe_2O_4$ and Fe_2O_4 in the flow of ferromagnetic nanofluid*, Eur. Phys. J. Plus, **132** (2017), 377.

19. P. J. Carreau, *An analysis of the viscous behavior of polymer solutions*, Can. J. Chem. Eng., **57** (1979), 135–140.

20. S. I. Abdelsalam, M. M. Bhatti, *New insight into AuNP applications in tumour treatment and cosmetics through wavy annuli at the nanoscale*, Sci. Rep., **9** (2019), 1–14.

21. Y. Yang, Y. Zhang, E. Omairey, et al. *Intermediate pyrolysis of organic fraction of municipal solid waste and rheological study of the pyrolysis oil for potential use as bio-bitumen*, J. Clean. Prod., **187** (2018), 390–399.

22. K. L. Hsiao, *To promote radiation electrical MHD activation energy thermal extrusion manufacturing system efficiency by using Carreau-Nanofluid with parameters control method*, Energy, **130** (2017), 486–499.

23. M. Khan, M. Azam, A. Munir, *On unsteady Falkner-Skan flow of MHD Carreau nanofluid past a static/moving wedge with convective surface condition*, J. Mol. Liq., **230** (2017), 48–58.

24. M. Waqas, M. I. Khan, T. Hayat, et al. *Numerical simulation for magneto Carreau nanofluid model with thermal radiation: A revised model*, Comput. Method. Appl. Mech. Eng., **324** (2017), 640–653.

25. M. Khan, M. Irfan, W. A. Khan, *Numerical assessment of solar energy aspects on 3D magneto-Carreau nanofluid: A revised proposed relation*, Int. J. Hydrogen Energ., **42** (2017), 22054–22065.

26. S. U. S. Choi, J. A. Eastman, *Enhancing thermal conductivity of fluids with nanoparticles*, In: *Proceedings of the 1995 ASME International Mechanical Engineering Congress and Exposition*, San Francisco, California, 1995, 99–105.

27. J. Buongiorno, *Convective transport in nanofluids*, J. Heat Trans., **128** (2006), 240.

28. M. I. Khan, S. Qayyum, T. Hayat, et al. *Entropy generation in radiative motion of tangent hyperbolic nanofluid in presence of activation energy and nonlinear mixed convection*, Phys. Lett. A, **382** (2018), 2017–2026.

29. S. S. Ghadikolaei, K. Hosseinzadeh, D. D. Ganji, *Investigation on Magneto Eyring-Powell nanofluid flow over inclined stretching cylinder with nolinear thermal radiation and Joule heating effect*, World J. Eng., **16** (2019), 51–63.

30. Y. Lin, Y. Jiang, *Effects of Brownian motion and thermophoresis on nanofluids in a rotating circular groove: A numerical simulation*, Int. J. Heat Mass Tran., **123** (2018), 569–582.

31. V. M. Falkner, S. W. Skan, *Some approximate solutions of the boundary-layer equations*, Philos. Mag., **12** (1931), 865–896.

32. H. T. Lin, L. K. Lin, *Similarity solutions for laminar forced convection heat transfer from wedges to fluids of any Prandtl number*, Int. J. Heat Mass Tran., **30** (1987), 1111–1118.

33. S. Nadeem, S. Ahmad, N. Muhammad, *Computational study of Falkner-Skan problem for a static and moving wedge*, Sensor. Actuat. B Chem., **263** (2018), 69–76.

34. F. A. Hendi, M. Hussain, *Analytic solution for MHD Falkner-Skan flow over a porous surface*, J. Appl. Math., **2012** (2012), 1–9.

35. M. S. Alam, M. A. Khatun, M. M. Rahman, et al. *Effects of variable fluid properties and thermophoresis on unsteady forced convective boundary layer flow along a permeable stretching/shrinking wedge with variable Prandtl and Schmidt numbers*, Int. J. Mech. Sci., **105** (2016), 191–205

36. M. Khan, M. Azam, A. S. Alshomrani, *Unsteady slip flow of Carreau nanofluid over a wedge with nonlinear radiation and new mass flux condition*, Results Phys., **7** (2017), 2261–2270.

37. H. Sardar, L. Ahmad, M. Khan, et al. *Investigation of mixed convection flow of Carreau nanofluid over a wedge in the presence of Soret and Dufour effects*, Int. J. Heat Mass Tran., **137** (2019), 809–822.

38. H. T. Basha, R. Sivaraj, A. S. Reddy, et al. *Impacts of temperature-dependent viscosity and variable Prandtl number on forced convective Falkner–Skan flow of Williamson nanofluid*, SN Appl. Sci., **2** (2020), 1–14.

39. H. T. Basha, R. Sivaraj, A. S. Reddy, et al. *SWCNH/diamond-ethylene glycol nanofluid flow over a wedge, plate and stagnation point with induced magnetic field and nonlinear radiation–solar energy application*, Eur. Phys. J. Spec. Top., **228** (2019), 2531–2551

40. W. Gao, M. Partohaghighi, H. Mehmet, et al. *Regarding the group preserving scheme and method of line to the numerical simulations of Klein–Gordon model*, Results Phys., **15** (2019), 1–7.

41. W. Gao, H. F. Ismael, S. A. Mohammed, et al. *Complex and real optical soliton properties of the paraxial non-linear Schrödinger equation in Kerr media with M-fractional*, Front. Phys., **7** (2019), 1–8.

42. W. Gao, H. F. Ismael, H. Bulut, et al. *Instability modulation for the (2+1)-dimension paraxial wave equation and its new optical soliton solutions in Kerr media*, Phys. Scr., 2019.

43. W. Gao, B. Ghanbari, H. Günerhan, et al. *Some mixed trigonometric complex soliton solutions to the perturbed nonlinear Schrödinger equation*, Mod. Phys. Lett. B, **34** (2020), 2050034.

44. A. Ciancio, *Analysis of time series with wavelets*, Int. J. Wavelets, Multi., **5** (2007), 241–256.

45. A. Ciancio, A. Quartarone, *A hybrid model for tumor-immune competition*, U. P. B. Sci. Bull. Ser. A, **75** (2013), 125–136.

46. A. Cordero, J. P. Jaiswal, J. R. Torregrosa, *Stability analysis of fourth-order iterative method for finding multiple roots of non-linear equations*, Appl. Math. Nonlinear Sci., **4** (2019), 43–56.

47. P. K. Pandey, *A new computational algorithm for the solution of second order initial value problems in ordinary differential equations*, Appl. Math. Nonlinear Sci., **3** (2018), 167–174.

48. H. Chen, J. Jiang, D. Cao, et al. *Numerical investigation on global dynamics for nonlinear stochastic heat conduction via global random attractors theory*, Appl. Math. Nonlinear Sci., **3** (2018), 175–186.

49. L. F. Shampine, I. Gladwell, S. Thompson, *Solving ODEs with MATLAB*, Cambridge University Press, Cambridge, 2003.

AIMS Press